

Response of Ni/Al laminates to laser-driven compression

C.T. Wei^a, V.F. Nesterenko^a, T.P. Weihs^b, B.A. Remington^c, H.-S. Park^c,
M.A. Meyers^{a,*}

^a University of California, San Diego, La Jolla, CA, USA

^b Johns Hopkins University, Baltimore, MD 21218, USA

^c Lawrence Livermore National Laboratory, Livermore, CA 94551, USA

Received 15 March 2012; accepted 18 March 2012

Available online 1 May 2012

Abstract

Ni/Al laminates with bilayer thicknesses in the micrometer ($\sim 5\ \mu\text{m}$) and nanometer ($\sim 50\ \text{nm}$) range were subjected to exothermic reactions induced by laser-driven compression. The initial shockless compression steepened into shock in the microscaled laminates generating a pressure pulse duration of several tens of nanoseconds, which induced strain rates varying from 10^7 to $10^8\ \text{s}^{-1}$. The laser energies applied, 650, 875, and 1305 J, generated peak compression stresses of 30, 75, and 118 GPa, respectively, at the plasma stagnated Al surface. Large differences in flow stresses and bulk compression moduli of Ni and Al introduced shear localization in the Ni/Al interfaces. The nanoscale Ni/Al laminates were fully reacted, producing NiAl with grain sizes less than 500 nm. The NiAl intermetallic phases, B2 (β) phase (fcc) and martensitic phase (bcc), coexist in the NiAl nanograins. It was confirmed that the intermetallic reaction in the Ni/Al microlaminate cannot self-sustain for the short duration, laser-driven compressive loading. The intermetallics NiAl (equiaxed grains) and NiAl_3 (dendrites) were identified on the plasma stagnated surface of Ni/Al microlaminates. The distribution of intermetallic phases varied according to the incident laser energies.

© 2012 Acta Materialia Inc. Published by Elsevier Ltd. All rights reserved.

Keywords: Laser; Nickel; Aluminum; Shock-induced reactions; Intermetallic phases

1. Introduction

Micro- and nanoscale Ni/Al reactive laminates have been used in a variety of different applications, for example the soldering of materials [1–3] by means of localized heating. Potential military applications utilizing the heat of exothermic reactions to enhance blast effects (<http://www.wired.com/science/discoveries/news/2002/12/56695>, <http://www.onr.navy.mil/Media-Center/Press-Releases/2002/Better-Warheads-Through-Plastics.aspx>) are also being considered. They have tailorable microstructures and remarkable mechanical and chemical properties: good corrosion resistance, high melting temperatures, low densities and high strengths of the intermetallic phases [3,4].

Reactions in Ni/Al reactive laminates release large amounts of exothermic heat for their intermetallic phases: $-150.6\ \text{kJ mol}^{-1}$ for NiAl_3 and $-118.4\ \text{kJ mol}^{-1}$ for NiAl [5]. These reactions can be easily ignited by laser heating [6], an electric current [7], or a thermal stimulus [8,9]. In past decades many approaches have been utilized to investigate these exothermic chemical reactions under extreme loading conditions. The intermetallic reactions induced by high pressure shock waves are classified as shock-induced and shock-assisted reactions according to the role of the shock wave in reaction initiation and propagation [10]. The shock wave-induced chemical reactions have extremely fast reaction velocities, 10^7 times faster than normal thermal reactions [11,12]. However, these two reaction mechanisms usually occur concurrently, thus increasing the uncertainty of defining the primary initiating mechanism of the intermetallic reaction under shock loading.

* Corresponding author. Tel.: +1 619 534 5698.

E-mail address: mameyers@ucsd.edu (M.A. Meyers).

Laser-driven shock waves have been used to investigate the dynamic behavior of materials [13–28]: aluminum [17,18], copper [19,20], tantalum [21,22], vanadium [23,24], iron [25,26], nickel [27], nickel aluminide [28,29], and nickel–aluminum laminates [13]. The laser beam, of high intensity $I_L > 10^{13} \text{ W cm}^{-2}$, generates strong ionization and thermal deposition on the irradiated surface, creating melting pools and craters [13]. Laser-driven shock waves in solid materials are generated by the rapid formation and expansion of a hot, dense plasma on the surface layer caused by direct irradiation by focused laser beams [14–16]. This method of generating shock waves using lasers is significantly affected by three factors: different laser absorption rates of the materials [16]; an inhomogeneous (Gaussian) laser intensity distribution caused by the focal spot of the laser beam [16]; a rapid decrease in the shock pressure in solids [13]. These phenomena have restricted the application of laser-driven shock compression. Direct laser-driven shock compression cannot maintain ultrahigh strain rate ($>10^6 \text{ s}^{-1}$) conditions in Ni/Al laminates for more than $\sim 10 \text{ ns}$ and introduces extended thermal damage on the irradiated surface, which renders the post-shock analysis complicated.

An innovative laser-driven shockless compression method was recently developed [17,18]. It enables an essentially smoother compression pulse propagating through the entire sample, which is similar to the “z-pinch” technique developed by Asay et al. [30]. This new approach generates compression by soft stagnation of the expanding plasma across a vacuum gap from a reservoir of polymer against the sample surface instead of direct laser irradiation of the exposed surface. Edwards et al. [17] and Lorenz et al. [18] conducted these laser-driven shockless compression experiments on aluminum samples in the Omega laser facility and proved that this approach induced quasi-isentropic compression stresses with amplitudes of 100–200 GPa within a 20–40 μm depth. This shockless compression was much less influenced by thermal heating than direct laser illumination of the sample. There are advantages to the study of the mechanical properties and phase transformations of bulk materials in a high stress, high strain rate and lower temperature regime. This laser-driven shockless compression has not previously been applied to study the chemical and mechanical response of reactive Ni/Al laminates. This is the primary objective of the research reported here.

2. Experimental methods

Ni/Al reactive laminates were subjected to laser-driven shockless compression using the Omega glass laser in the Laboratory for Laser Energetics at the University of Rochester. In order to investigate the behavior of the Ni/Al reactive laminates under the aforementioned loading conditions the 351 nm wavelength laser [31] with energies of 1305, 875 and 650 J was used to produce an expanding dense plasma which generated laser-driven shockless compression in the laminates. The laser pulse duration was 3.7 ns and the

intensity varied from $\sim 3.8 \times 10^{12}$ to $\sim 7.6 \times 10^{12} \text{ W cm}^{-2}$. The shockless compression produced by stagnation of the high density plasma was applied to the Ni/Al laminates having a nanoscale Ni/Al laminate structure (bilayer thickness 54 nm) sandwiched between two microscale laminates (bilayer thickness 5 μm). Samples were enclosed in a hollow tube with a 6 mm inner diameter and a length of 3 cm which was filled with aero-gel, as shown in Fig. 1a. A removable cap with a centered 4 mm hole was used to clamp and fix the sample at the front end of the tube (Fig. 1a).

There are three stages in generating shockless compression using an expanding plasma. First, the incident laser energy flux is converted in the ablator–reservoir to a low density plasma [17]. In the second stage, after plasma generation, it expands across the vacuum gap. In the third and final stage the plasma stagnates and piles up against the front surface of the laminate, producing a monotonically rising pressure. The amplitude of the pressure wave propagating into the laminates gradually increases and steepens to form a shock wave. This three-step approach to loading the sample isolates the sample from laser heating effects.

The micro- and nanolaminates were prepared by accumulative roll bonding [32] and magnetron sputter deposition [1–3], respectively. Two microscale laminates which had a total thickness $\sim 0.85 \text{ mm}$ were machined into 5 mm disks with three $\sim 0.3 \text{ mm}$ well-aligned screw holes used to sandwich a nanoscale laminate of 54 nm bilayer thickness, giving a total thickness of 8.5 μm , as shown in Fig. 1b. The sandwich structure was assembled and fixed to a 300 μm thick tungsten washer (which formed the gap required for this shockless loading technique) with an outer diameter of 10 mm and inner diameter of 2 mm. A 3 mm diameter and 20 μm thick polycarbonate ablator ($\text{C}_{16}\text{H}_{16}\text{O}_4$), density 1.2 g cm^{-3} , and a 180 μm thick brominated polystyrene reservoir ($\text{C}_{50}\text{H}_{48}\text{Br}_2$), density 1.23 g cm^{-3} , were placed on the laser irradiated front surface of the tungsten washer (Fig. 1b). The tungsten washer, with a machined radial groove for the vacuum pump (dashed line in Fig. 1b), was clamped between the cap and the front end of the tube. The radial groove was designed to allow the creation of a vacuum between the ablator–reservoir and the front surface of the sandwich laminates.

The as-produced and recovered samples were characterized and analyzed using a scanning electron microscope (Philips XL30 ESEM), scanning/transmission electron microscope (EFI Titan 80–300 kV S/TEM) and the energy-dispersive X-ray spectroscopy (EDX). The dynamic response of the laminates and the shock-wave propagation in this bulk material were estimated using the one-dimensional radiation hydrodynamics code HYADES.

3. Results and discussion

3.1. Initial structure of micro- and nanolaminates

Cross-sections of the Ni/Al micro- and nanolaminates before being shock loaded are presented in Fig. 2. The

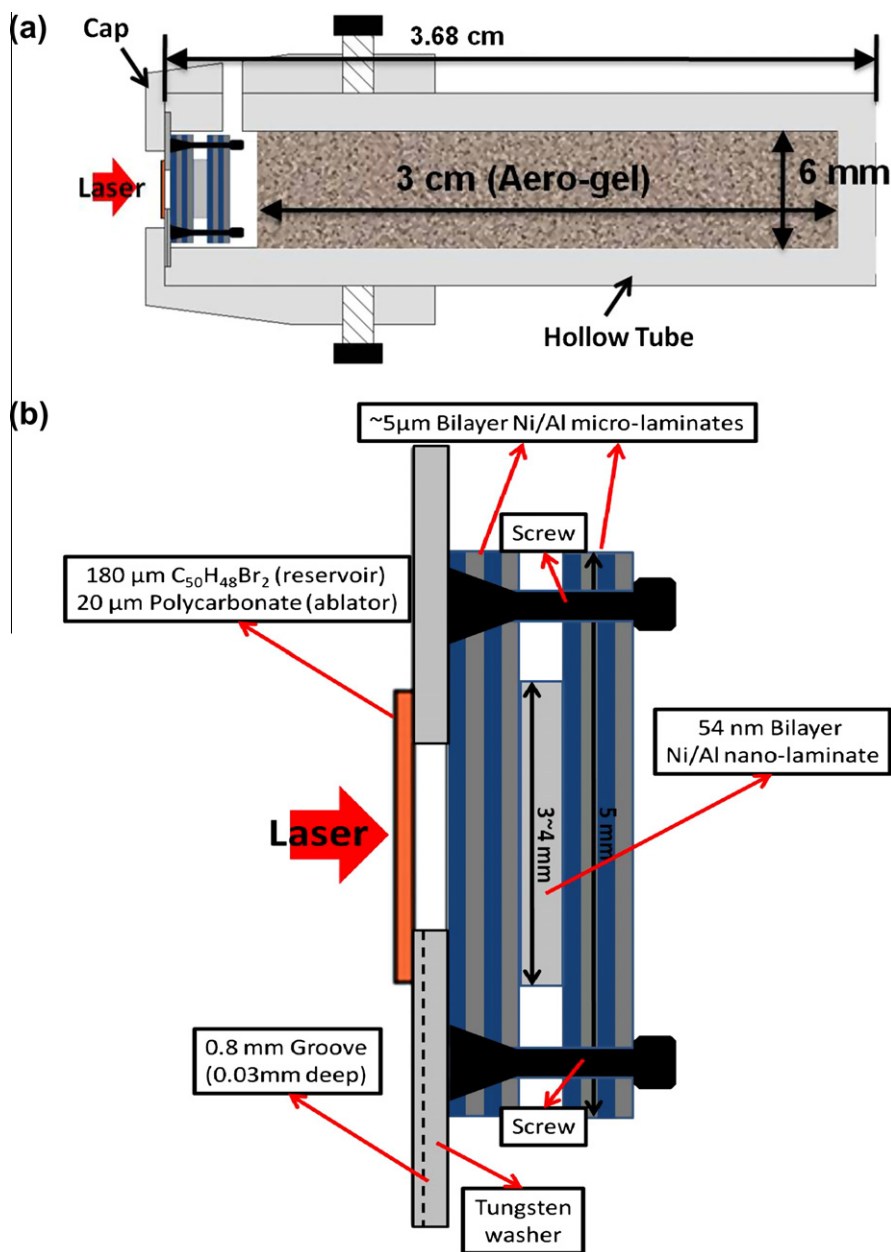


Fig. 1. (a) Sample holder for OMEGA laser experiments with assembly containing laminar samples. (b) Schematic of the three layers of laminates with polycarbonate ablator and tungsten washer; Two Ni/Al micro-laminates with 5 μm bilayer thickness sandwich an 8.5 μm thick nano-laminate with 54 nm bilayer thickness.

irregularly lamellar microlayers of Ni (lighter) and Al (darker) sheets forming an $\sim 5 \mu\text{m}$ bilayer (Fig. 2a) were made by an accumulative roll bonding (cold rolling) process, described in Wei et al. [13]. The molar ratio of the microlaminate is Ni:Al = 1:1. The nanoscale Ni/Al laminate (Fig. 2b) was fabricated by a magnetron sputtering process. It had a well-defined Ni (lighter) and Al (darker) periodic multilayer structure characterized by a 54 nm average bilayer thickness. The total thickness of the Ni/Al nanolaminate was about 8.5 μm . Alternatively, the deposited Ni and Al layers had a thickness ratio of 2/3 and the corresponding stoichiometric ratio was about 1/1 for Ni/Al.

The Ni/Al microlaminate was sectioned perpendicularly to the rolling direction and then thinned by an ion milling process for transmission electron microscopy (TEM). Fig. 3 shows bright field (Fig. 3a and c) and corresponding dark field (Fig. 3b and d) TEM micrographs of the layers generated by the accumulative roll bonding process. The structure of the aluminum lamellae consists of approximately equiaxed grains which are less than 25 nm across. There are a large number of defects in the Al nanograins caused by severe plastic deformation. The associated selected area diffraction shown in the inset in Fig. 3a reveals sharp diffraction rings and dots reflecting the Al

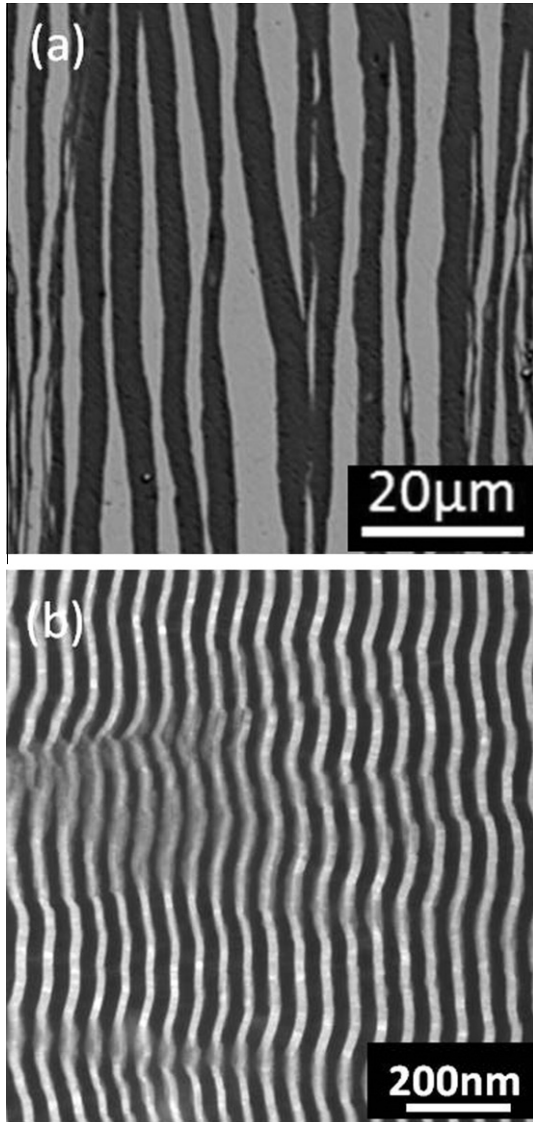


Fig. 2. Cross-sections of (a) cold-rolled Ni/Al micro-laminate (SEM) and (b) nano-laminate fabricated by the magnetron sputter deposition (STEM).

polycrystalline structure and halo diffraction rings indicating possible nanocrystalline structure caused by the accumulative roll bonding process [33].

The TEM micrographs of the Ni layer from the microlaminate are shown in Fig. 3c and d. They reveal elongated grains with a high density of dislocations. In contrast to Al, there was no complete recrystallization. The width of the Ni grains measured from the dark field TEM image (Fig. 3d), varied from less than 100 to over 500 nm. The selected area diffraction pattern (Fig. 3c) has elongated spots which indicate that the Ni crystal has a significant amount of strain caused by the accumulative roll bonding process.

Focused ion beam (FIB) milling was utilized to prepare the TEM sample of the magnetron sputter deposited Ni/Al nanolaminate with the microstructure shown in Fig. 4a and b. A platinum layer was deposited prior to FIB milling, as shown in the top right of Fig. 4a. The Al layer is composed

of columnar single crystal domains with a width of ~20 nm; the Ni layer had single crystal columns with a width greater than 10 nm. The magnified high resolution image of the interface region indicated by the square in Fig. 4a is presented in Fig. 4b. It reveals a clear Al [1 $\bar{1}$ 0] mono-crystalline structure and moiré fringes corresponding to the interaction due to differences in crystal orientations between adjacent Al grains. The high resolution TEM micrograph in Fig. 4b shows that the deposited Ni/Al laminate was fully dense with a very low dislocation density.

3.2. HYADES simulation

The use of laser-driven shockless compression significantly decreases undesirable effects by reducing thermal deposition on the irradiated surface and rapid attenuation of the shock pressure in the solid. These are two critical problems of direct laser shock experiments [13]. The schematic in Fig. 5a presents the evolution of the laser beam–laminate sandwich interaction. The initial experimental set-up is presented on the left side of Fig. 5a. The laser beam irradiates the ablator–reservoir slab generating an energetic plasma which expands across the vacuum gap and stagnates on the front surface of the sandwich laminates, as shown in the center of Fig. 5a. This results in shockless compression which propagates to a depth of ~20–40 μm. The compression wave steepens and develops into a shock wave propagating through the laminates and creating a crater, spall, and fragments on the recovered Ni/Al sandwich laminates, shown schematically on the right side of Fig. 5a. Wei et al. [13] demonstrated that limited reaction occurred in direct drive laser compression of microlaminates.

The hydrodynamic computational code HYADES was used to estimate the mechanical response of laminates to shockless compression. Remington et al. [34] conducted similar experiments and found that the compression pressure induced by plasma stagnation can be represented by the equation:

$$P \propto \frac{\omega^{0.5} I^{0.76}}{t^{0.13}} \quad (1)$$

where ω , I and t are the laser frequency, intensity and pulse duration, respectively. Edwards et al. [17] measured the velocity at the rear surface of Al samples and back integrated using the Al equation of state to obtain the time-dependent pressure profile at the front surface. The input compression profiles at the front surface of the sandwich laminates were subtracted and scaled from the work of Edwards et al. [17] using Eq. (1) with a similar experimental set-up. The results are shown in Fig. 5b.

These input pressure profiles acting at the front surface were applied as HYADES pressure sources. The Steinberg shear model and Steinberg–Guinan high strain rate elastic–plastic model [36] were incorporated into the computation in order to estimate the mechanical response of the Ni/Al

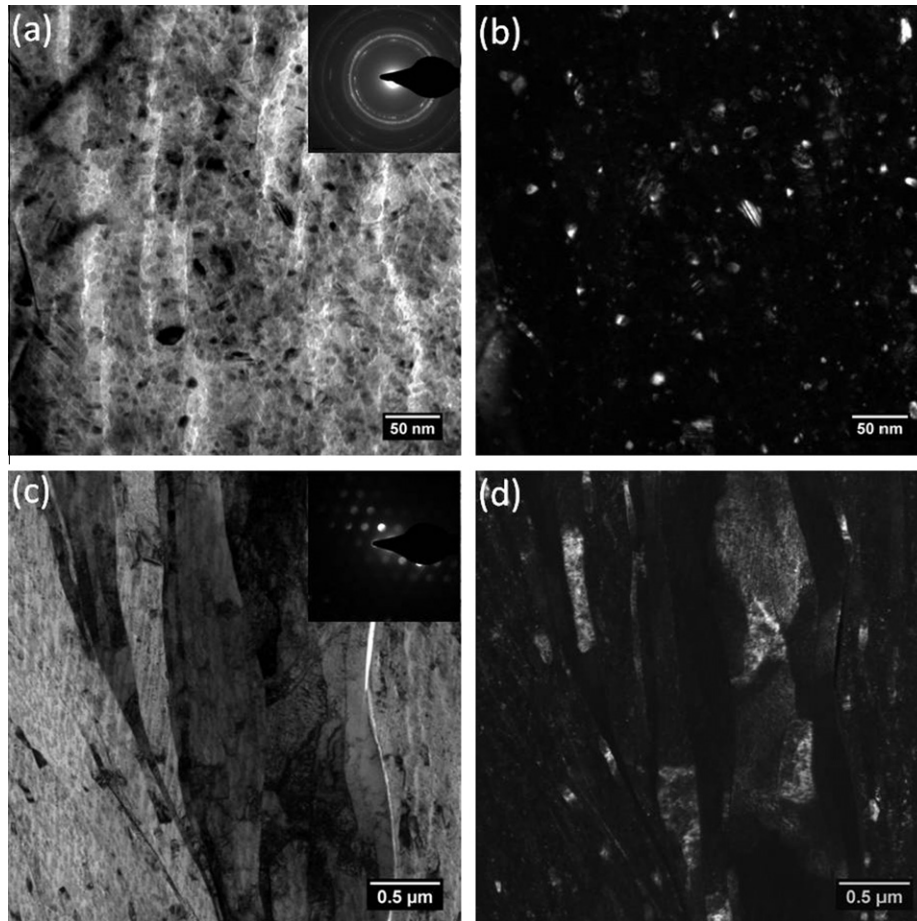


Fig. 3. TEM micrographs of Ni/Al micro-laminate prior to shock: (a) Bright field with diffraction pattern, and (b) dark field images of the cold-rolled Al phase; note the nanoscale equiaxed grain structure. (c, d) Same for the Ni phase; note elongated grains resulting from cold rolling.

laminates. Fig. 5c shows that fully developed shock waves propagated into the microlaminates after traveling through the shockless compression region. Elastic wave precursors appear in the earlier stages of the shock waves (Fig. 5c) due to the extremely high strain on the plasma stagnated surface [30,37]. The pressure waves generated by laser-driven, shockless compression at three different laser energies have relatively weak attenuation of the peak pressure in the Ni/Al laminates. For instance, the peak pressure of the 650 J laser-driven shockless compression waves shows less than 20% attenuation for a thickness of ~ 0.85 mm while propagating in the Ni/Al laminate, which is significantly smaller than in direct laser shock experiments, which show an attenuation of $>90\%$ over the same thickness [13], as shown in Table 1. This semi-steady shock wave propagated through the first Ni/Al microlaminate and was conveyed to the nanoscale laminate. The shock wave pressure is effectively retained in the nanolaminate for about 70 ns and the peak pressure can reach 28 GPa for the 650 J laser experiment, with a 20% variation between the front and the rear surfaces of the nanolaminate, as shown in Fig. 5d. The peak pressures on the front microlaminate P_M and the nanolaminate P_N for each specific laser

condition are listed in Table 1 with the variations ΔP_M in the peak pressures in the microlaminate.

HYADES one-dimensional simulation results show that the estimated highest strain rates can reach $\sim 10^6$ – 10^7 s^{-1} in the middle of the front microlaminate, which is consistent with Edwards et al. [17] and Lorenz et al. [18], and $\sim 10^8$ s^{-1} in the nanolaminate. The strain rates are established by dividing the strain at the maximum pressure by the rise time of the wave front. This has been established by a combination of VISAR diagnostics and computations in previous studies. We have confidence in the reliability of these values. Independent experiments were executed on each shot day to verify the “drive” (applied pressure vs. time) used in the simulations. From the plots of simulated plastic strain vs. time $e_p(t)$ the estimated strain rates correspond to de_p/dt , which is accurate to 20–30% [18,35]. Higher precisions can be obtained, but require carrying out the analysis in two dimensions.

The increased strain rate is due to the compression pulse “shocking up” as it travels through the material. The variation in the highest strains of the Al and Ni layers was negligible in the laminates in the 650 J laser experiment, however, the total strain in the Al layers was twice that

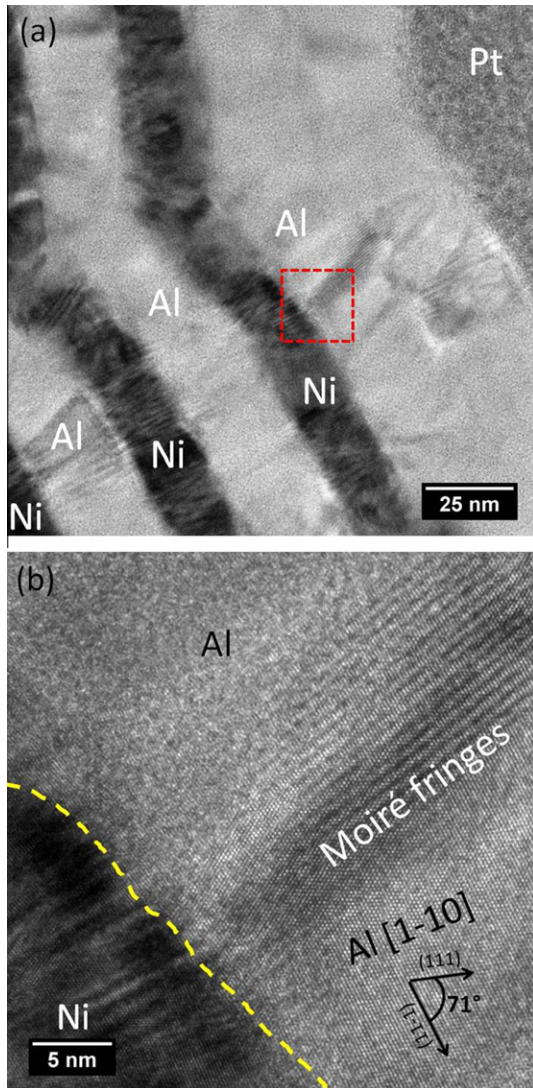


Fig. 4. TEM micrograph of nano-laminate prior to shock: (a) Single crystal domains are columns normal to Ni–Al interface; (d) moiré fringes on the Al and Ni phases due to the overlap of two misoriented crystal planes.

for the Ni layers in the 1305 J laser experiment, which is due to the higher strain hardening exponent of Ni compared with Al in the Steinberg–Guinan model [36]. This resulted in a higher flow stress of the nickel while compressing the sample and a significant decrease in the total strain in the nickel layer. The corresponding bulk moduli are 180 GPa for Ni and 76 GPa for Al. The evidence on the cross-sections of the original (Fig. 2a) and recovered samples (Fig. 6f) shows that the recovered sample has relatively thinner Al layers compared with the original laminate. Details of the highest strain in the middle Al and Ni layers in the front microlaminate are shown in Table 2.

3.3. Structure of the laser compressed laminates

As mentioned in Section 2, the kinetic energy of the laser generated plasma produced a compression pressure wave,

which developed into a shock wave propagating in the laminates. Craters were found on the front surface exposed to plasma, as shown in Fig. 6a. Spalls were found on the rear free surface, as shown in Fig. 6b. Similar fractures were found in direct laser shock compression experiments [13,38]. The 1305 J laser also created a crater on the front surface (Fig. 6c). The sandwich structure was shattered into small segments due to the strong reflected tensile stress, which pulled apart the laminates, especially in the high laser energy experiment. The fracture mechanisms and morphologies are not addressed here. However, these were carefully characterized in the previous studies [13,38]. Laser-driven initially shockless compression incorporating a sandwich structure of Ni/Al laminates reveals significant phenomena, which are described for the first time.

3.3.1. Intermetallic reactions in recovered samples

Reaction products in the form of granules and dendrites were found on the front surface of the microlaminates exposed to stagnated plasma in all the experiments (Fig. 6a and c). At the spall surface there was no intermetallic phase nor any intermixing regimes, as shown in Fig. 6b and the inset. At the crater center in Fig. 6d NiAl intermetallic granules were found in the plasma stagnated region in the 1305 J laser experiment. These results suggest that the laser energy plays an important role in the intermetallic reactions.

SEM observations conducted on cross-sections of the plasma stagnated microlaminates from three different experiments were used to distinguish the intermetallic distributions corresponding to different laser energies. Fig. 7 shows the schematics of the phase distributions observed on the plasma stagnated microlaminates for the three different laser energies. It should be noted that fractures such as cracks and voids are not illustrated in the plots. The 650 J laser experiment had only NiAl₃ dendrites in a limited area of the front microlaminate. A small number of NiAl grains on the front surface and a considerable quantity of NiAl₃ dendrites were observed in the cross-section of the plasma stagnated microlaminate in the 875 J laser experiment. The 1305 J laser experiment revealed fully reacted NiAl grains in the central area, while the lateral regions were completely filled by NiAl₃ intermetallic dendrites, as shown in Fig. 7 (1305 J laser).

SEM observations of cross-sections of the front microlaminate are shown in Fig. 8 for the 1305 J laser experiment. Fig. 8a presents different intermetallic phases with distinct morphologies and compositions. In the center of the crater (Fig. 8b) the Ni/Al laminate fully reacted and formed equiaxed NiAl intermetallic grains with grain sizes of from 2 to 7 μm . The NiAl intermetallic phase was identified by EDX and had a 53:47 Ni:Al atomic ratio, consistent with the Ni–Al phase diagram [39]. In the regions adjacent to the center (Fig. 8c) the NiAl₃ intermetallic dendrites grew perpendicularly to the aluminum layer identified by EDX analysis. This is similar to our previous findings [13]. It can be speculated that this type of reaction initiates from the

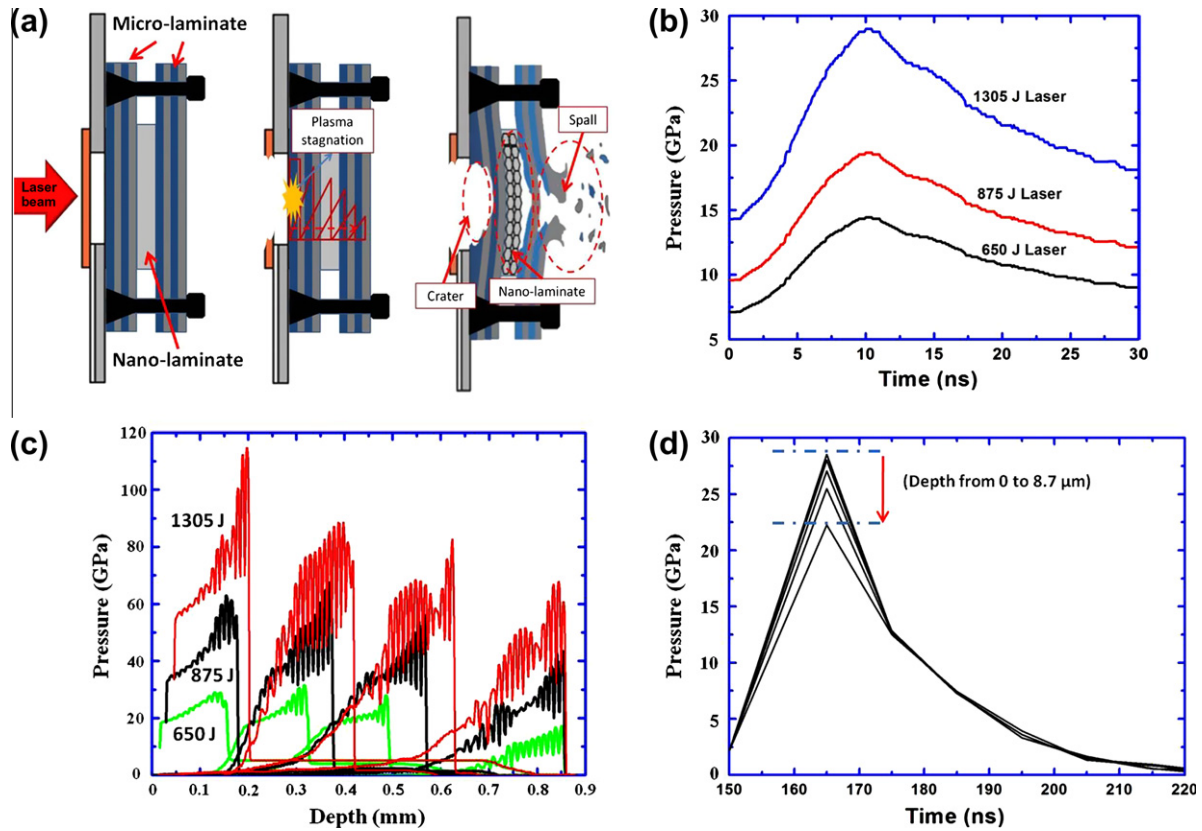


Fig. 5. (a) Schematic illustrating, from the left to the right: original sandwich sample; plasma stagnation induced by laser beam and a formation of the shock-less compression; shock wave reflecting at back surface as tensile pulse creating spalling and fragmentation. (b) Input pressure profiles scaled from [16]. (c) Propagation of compression pulse at increasing depths into the micro-laminate. (d) Compression pressures vs. time in the nano-laminate.

Table 1
Parameters in the laser compression experiments.

E_L (J)	I_L (W cm^{-2})	t (ns)	P_M (GPa)	ΔP_M	P_N (GPa)	Δ (μm)
650	3.8×10^{12}	3.7	30	16%	29	300
875	5.1×10^{12}	3.7	75	27%	59	300
1305	7.6×10^{12}	3.7	118	29%	99	300
430 ^a	1.28×10^{13a}	3 ^a	$\sim 180^a$	$>90\%^a$		0

E_L , total laser energy; I_L , laser intensity; t , laser pulse duration; P_M , peak pressure in the front microlaminate; ΔP_M , variation of the peak pressures in the microlaminate; Δ , gap width between the reservoir and the front surface of the Ni/Al microlaminate.

^a Taken from Wei et al. [13].

interfacial interaction caused by localized shear due to the differences in bulk compression moduli and flow strength of Ni and Al. The NiAl₃ intermetallic phase was the first stable phase to appear when cold rolled Ni/Al microlaminates were slowly heated [40], and formation can initiate at a relatively low temperature ~ 300 – 500 °C [8]. At a region farther away from the center of Fig. 8d no intermetallic phase was found, however, at the interface of the Ni and Al layers vortices, intermixing, and localized shear were observed. We identify these features as the initial stage of mechanical alloying in the microlaminate due to significant difference in the bulk compression moduli of Ni and Al.

The cross-section of the front microlaminate obtained from the 650 J laser experiment had only a small number

of NiAl₃ intermetallic dendrites with the same morphology as in Fig. 8c, from the top bilayer down to a depth of <10 μm. The dendrites were sectioned and analyzed using EDX mapping analysis embedded in the STEM system. Fig. 9 shows the EDX mapping results, which indicate that the NiAl₃ phase (from A to B) has a relatively uniform composition of Ni:Al of about 40:50 (wt.%), regardless of the 10 wt.% of impurities, corresponding to an atomic ratio of 1:3 Ni:Al. The EDX mapping results in the Al matrix (from B to C) show that Ni diffuses into the Al matrix, however, the gradual increase in Al and decrease in Ni (wt.%) suggest that the uniform composition of the intermetallic is not formed in this regime. Deeper into the specimen there are intermixing, vortices and extrusion of the molten Ni, shown in Fig. 8d. This image was taken in an

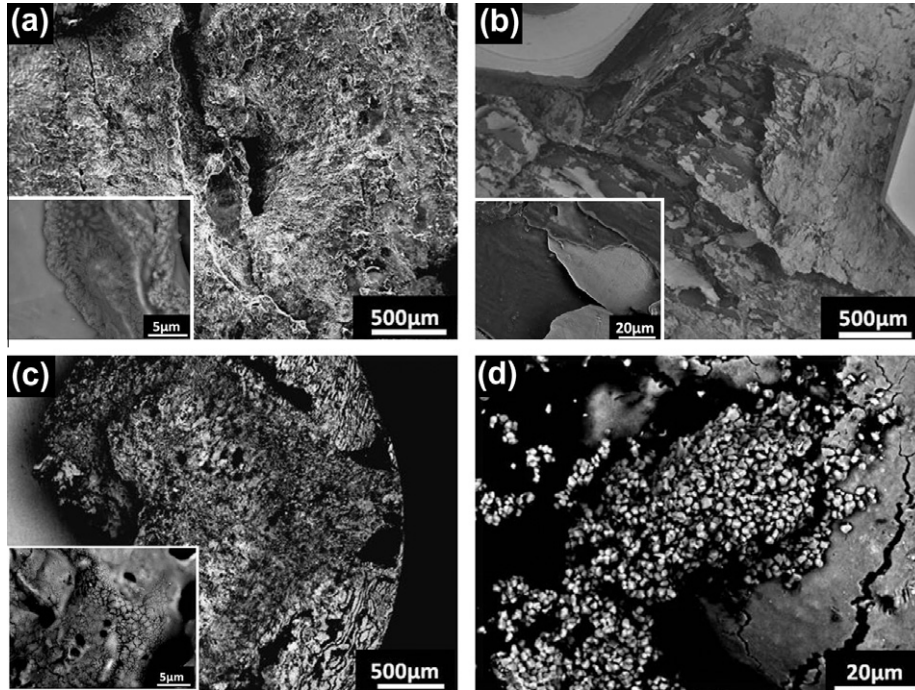


Fig. 6. Surface morphologies of recovered micro-laminate samples for (a, b) 650 J and (c, d) 1305 J laser experiments. (a) Crater on the front (plasma exposed) surface for 650 J with intermetallic dendrites on the crater in inset; (b) spallation on the rear surface of second micro-laminate for 650 J with separation of laminae and ductile failure edges in inset; (c) crater on the plasma exposed surface for 1305 J with intermetallic dendrites in inset; (d) granular reaction products in center of crater for 1305 J laser.

Table 2

Highest strain in the Al and Ni layers in the middle of the front microlaminate (obtained from HYADES simulations).

Laser condition (J)	Highest strain (Al)	Highest strain (Ni)
1305	0.713	0.409
875	0.520	0.263
650	0.311	0.29

area away from the indented center of the plasma stagnated microlaminate (1305 J laser experiment). It should be noted that in this unreacted area the aluminum thickness was drastically reduced, as shown in Fig. 8d, which is consistent with the HYADES results in Section 3.2. The recovered sample from the 875 J laser experiment had a small number of NiAl intermetallic grains, and the NiAl₃ dendrites propagated inward to a depth of 100 µm in the center of the plasma stagnated areas. In the areas underneath the bilayers with NiAl₃ dendrites the vortices, extrusion of molten Ni and shear were also found, as well as the laminar structure with reduced Al layers.

The distribution of intermetallic phases in the recovered samples of the front microlaminates of the laser-driven and initially shockless compression experiments revealed critical features of the reaction stages of self-sustaining high temperature synthesis (SHS). SHS can be initiated in the Ni/Al reactive laminate by a simple electrical spark, a flame [1–3,40], or a laser heating source [6]. Qiu et al. [40] defined the Ni/Al reaction in microscale Ni/Al as two sequential steps: the first reaction generates the NiAl₃ intermetallic

phase and propagates laterally over the surface of the laminate at a relatively slow rate; the second reaction consumes the remaining Ni and converts the NiAl₃ intermetallic into NiAl. The second reaction is an exothermic chemical reduction process which releases a large quantity of heat and facilitates the SHS reaction. However, in the current study the NiAl intermetallic phase was formed in the plasma-stagnated crater center in the 1305 J laser experiment, and there was no reaction at the edge of the microlaminate. This suggests that the intermetallic reaction did not propagate through the entire sample, despite the fact that the final intermetallic phase, NiAl, was detected in the center of the front microlaminate (Fig. 8a).

The Ni/Al nanolaminate was converted to a fully reacted NiAl phase with equiaxed grains having an average size of 0.5 µm in all three laser conditions, as shown in Fig. 10a and b for the 650 J laser experiment. Fully reacted Ni/Al nanolaminate was produced by the shock-wave loading regardless of the input of external thermal energy. These NiAl intermetallic grains resulted in undulating features (inset in Fig. 10a) which are characteristic of self-sustaining reactions in nanolaminates [7]. The self-sustaining reaction in the Ni/Al nanolaminate generated a large amount of heat, resulting in melting of the adjoining unreacted microlaminate. This is shown in Fig. 10b, however, no intermetallic reaction was found in the back microlaminate, showing that the reaction did not propagate from the nanolaminate to the microlaminate.

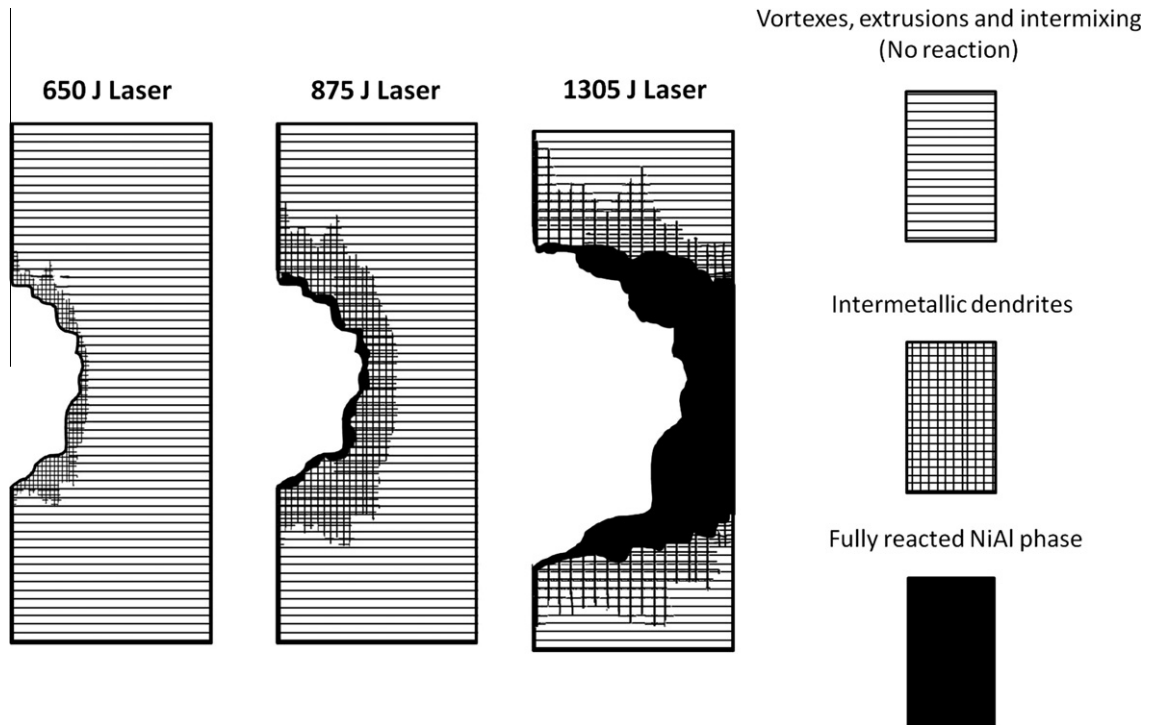


Fig. 7. Schematic representation of cross sections of recovered micro-laminates (front samples) with phase distribution.

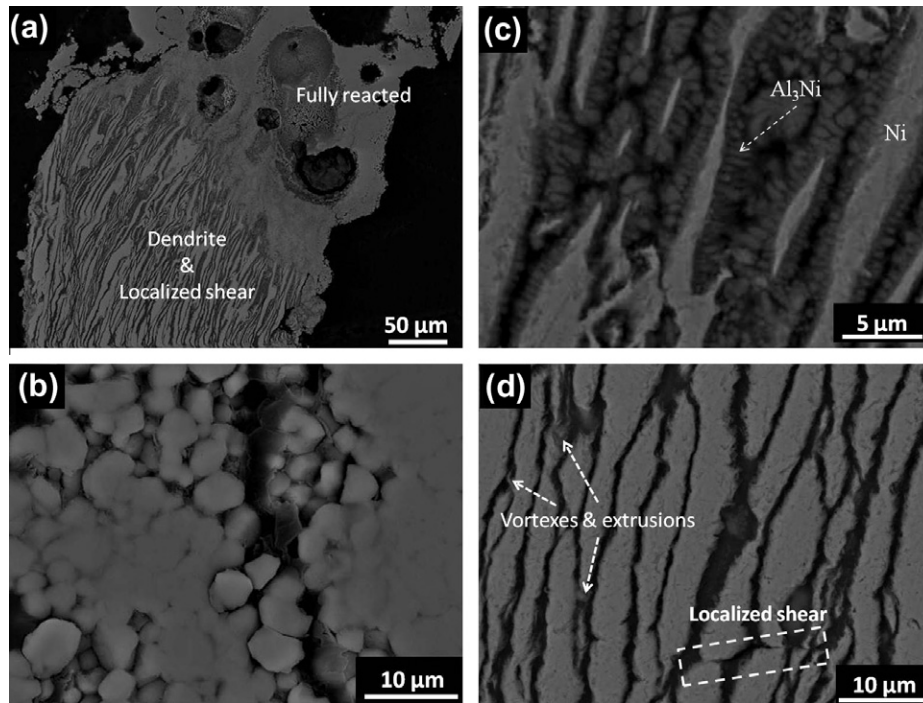


Fig. 8. Cross-sectional views of recovered micro-laminate (irradiated surface layers from 1305 J laser experiment); (a) overall view of specimen; (b) detailed view of NiAl spherules resulting from interfacial reaction between Ni and Al layers (similar to [15]); (c) NiAl₃ elongated spherules growing perpendicular to interface by mechanism presented in [13] (a); (d) shock-less compression-induced intermixed extrusions, vortexes, and localized shear due to the inhomogeneities in compression pressures and wave velocities.

3.3.2. Thermodynamic and kinetic analysis

The adiabatically self-sustaining reaction in the nano-scale Ni/Al laminate was driven by exothermic heat at the reaction front [1–3,5,7–9,41], which increased the

temperature and introduced a propensity for intermetallic reactions. Thermodynamic equations were used to estimate the maximum temperature achieved in each particular exothermic reaction corresponding to specific intermetallics

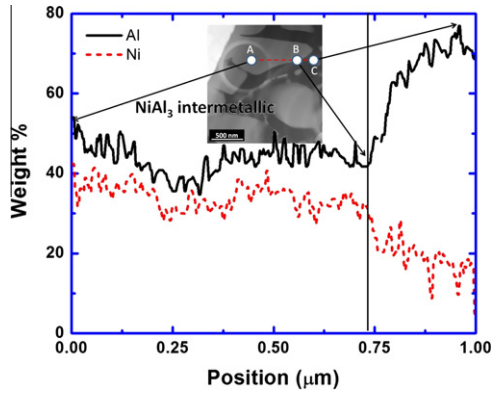


Fig. 9. STEM-EDX analysis: the scanning line is shown on the STEM image as the dash line on the micrograph, crossing the interface between intermetallic and Al phase; intermetallic phase is NiAl_3 and the compositional distribution in the grain is quite uniform.

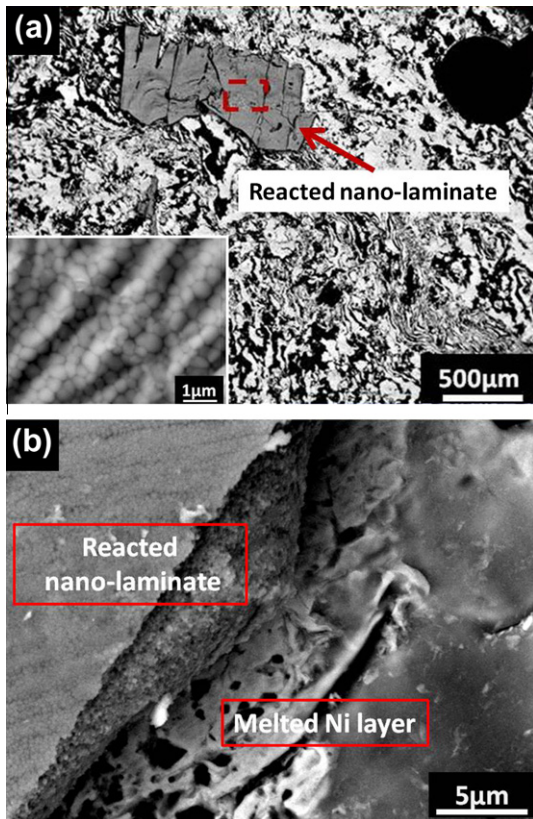


Fig. 10. Nano-laminate, 650 J experiment; (a) granular intermetallics in the reacted nano-laminate; (b) melted and resolidified Ni layer formed adjacent to a reacted nano-laminate intermetallic as a result of heat released from reaction.

such as NiAl and NiAl_3 . The following equation was used to estimate the maximum final temperature T_{max} in the solid state:

$$\begin{aligned} \Delta H_{T_0}(\text{Ni}_x\text{Al}_y) + \int_{T_0}^{T_r} (C_p(\text{Ni}) \cdot x + C_p(\text{Al}) \cdot y) dT \\ = \int_{T_r}^{T_{\text{max}}} C_p(\text{Ni}_x\text{Al}_y) dT \end{aligned} \quad (2)$$

where $\Delta H_{T_0}(\text{Ni}_x\text{Al}_y)$ is the heat of formation at T_0 (K), which is 298 K, $C_p(\text{Ni})$, $C_p(\text{Al})$ and $C_p(\text{Ni}_x\text{Al}_y)$ are the specific heat capacities of Ni, Al, and Ni_xAl_y , respectively, and T_r is the reaction temperature. Details of the thermodynamic parameters are shown in Table 3 [5,42]. T_r was chosen to be 600 K according to Ma et al. [7]. It is found that the estimated final temperature is sufficient to melt the intermetallic phase and the surrounding reactants. For instance, the NiAl adiabatic reaction can reach $T_{\text{max}} \sim 3700$ K. This suggests that the intermetallic and surrounding reactants can be at least partially melted while the exothermic reaction is progressing. This facilitates the sequential reactions and results in SHS.

The intermetallic reactions in the Ni/Al laminates are significantly influenced by the heat dissipation rate, the intermixing of layers [1–3,8], and the bilayer thickness [1–3]. Ma et al. [7] proposed an energy balance model which was used to estimate the maximum bilayer thickness required for SHS at ambient temperature. In this approach the rate of heat generation should be faster than the sum of the rates of the heat absorption by the materials $C \frac{dT}{dt}$ and the heat dissipation $\frac{dE}{dt}$ at the reaction front due to conduction and radiation. The inequality is:

$$\frac{dH_{T_0}}{dt} > C \frac{dT}{dt} + \frac{dE}{dt} \quad (3)$$

where H_{T_0} , C , T , t and E are the heat generated at ambient temperature, specific heat capacity, temperature, time, and dissipated heat, respectively. The heat generation rate can be re-written as:

$$\frac{dH}{dt} = \left(\frac{\Delta H_{T_0}}{L} \right) R(T) \quad (4)$$

where ΔH_{T_0} is the heat generation per unit volume from the exothermic reaction, L is the bilayer thickness, and $R(T)$ is the temperature-dependent reaction rate. By substituting Eq. (4) into Eq. (3) and considering that in the limit there is insufficient heat generation to increase the surrounding temperature (and thus the temperature increase dT/dt can be neglected) Ma et al. [7] obtained the inequality:

$$L_{\text{max}} = \frac{\Delta H_{T_0} \times R(T)}{dE/dt} \geq L \quad (5)$$

Eq. (5) establishes the limits of the maximum thickness of the bilayer for the self-propagating high temperature reaction at a given temperature and reaction rate at the reaction front.

Wang et al. [1] and Gunduz et al. [41] investigated SHS of the NiAl intermetallic. The plots of reaction velocity vs. bilayer thickness from Wang et al. [1] and Gunduz et al. [41] are shown in Fig. 11. It demonstrates that an increase in the bilayer thickness L results in a decrease in the reaction speed. The increase in bilayer thickness also corresponds to a slower heat dissipation rate dE/dt . However, at the reaction front the heat dissipation rate is a function of the reaction temperature T and the ambient temperature T_0 . Ma et al. [7] proposed that without increasing the

Table 3
Heats of formation and specific heat capacities for NiAl and NiAl₃ [7,42].

Reactant or intermetallic	$\Delta H_{298\text{ K}}$ (kJ mol ⁻¹)	Specific heat capacity (J mol ⁻¹ K ⁻¹)
Al		$20.108 + 13.166 \times 10^{-3}T + 0.033 \times 10^5 T^{-2}$
Ni		$19.355 + 22.456 \times 10^{-3}T + 0.017 \times 10^5 T^{-2}$
NiAl	-118.407	$41.925 + 13.6 \times 10^{-3}T - 0.033 \times 10^5 T^{-2} + 0.1 \times 10^{-6} T^2$
NiAl ₃	-150.7	$43.144 + 138.406 \times 10^{-3}T + 14.611 \times 10^5 T^{-2} - 67.314 \times 10^{-6} T^2$

ambient temperature T_0 the maximum bilayer thickness for SHS was restrained. The empirical results [1–3,7] and the estimation from the plot in Fig. 11 show that the maximum reaction length of NiAl SHS is less than 100 nm at ambient temperature (~ 298 K). This is consistent with the results in this study, where formation of the fully reacted NiAl phase in the Ni/Al microlaminate did not result in SHS propagating through the entire sample.

3.3.3. Morphologies of the nanoscale structure of intermetallics

The nanolaminate fully reacted for the three laser energies. Equiaxed NiAl with grain sizes varying from 200 to 400 nm are shown in the TEM micrographs in Fig. 12a (bright field) and Fig. 12b (dark field). A simple diffusion-controlled grain growth equation can be applied to estimate the grain growth time of NiAl [43]:

$$t = \lambda^2 / \tilde{D}_{\text{NiAl}} \quad (6)$$

where t is the growth time, λ is the average diameter of the NiAl grain and \tilde{D}_{NiAl} is the interdiffusion coefficient of the NiAl intermetallics, which can be calculated using the Arrhenius equation:

$$\tilde{D}_{\text{NiAl}} = \tilde{D}_{0\text{NiAl}} \times \exp\left(\frac{-\tilde{Q}_{0\text{NiAl}}}{RT}\right) \quad (7)$$

where the pre-exponential factor and the activation energy are obtained from [39] $\tilde{D}_{0\text{NiAl}} = 3.7 \times 10^{-2} \text{ m}^2 \text{ s}^{-1}$ and $\tilde{Q}_{0\text{NiAl}} = 358 \text{ kJ mol}^{-1}$, respectively, R is the gas constant, and T is the temperature at the reaction front. For the adiabatic reaction of the Ni/Al nanolaminate investigated in

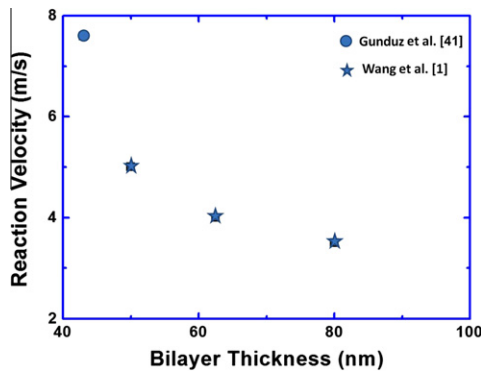


Fig. 11. Reaction velocities for self-sustaining high temperature synthesis in nanoscaled Ni–Al laminates as a function of bilayer thickness (from Wang et al. [1] and Gunduz et al. [41]).

this study the exothermic reaction can increase the temperature to about 1900 K [5]. The growth time is orders of magnitude ($\sim 10^4 \times$) higher than the laser transit time. Thus the nanosized grain structure is thought to form after passage of the shock wave. The measured grain size is ~ 300 nm. An estimated grain growth time 1.58×10^{-2} s, is obtained.

The atomic resolution image presented in Fig. 12c reveals the structure of the NiAl grains ($d \approx 300$ nm). The corresponding fast Fourier transform (FFT) image in the inset of Fig. 12c shows a diffraction pattern of the NiAl $Pm3m$ (001) surface. Lattice defects are seen in the NiAl nanograins, which can be seen as randomly distributed shadows in the brighter grains of Fig. 12a and b. They have the same zone axis $\langle 001 \rangle$ in the bright field image and the corresponding dark field image. Fig. 12d shows two vacancies, as well as partial and complete dislocations. It should be noted that clustered areas of point defects were also observed in the atomic resolution micrograph and these, as well as vacancies, are commonly found in the materials quenched from near melting temperature [44]. Two different phases of the NiAl intermetallic, the β -phase (fcc structure) in Fig. 12e and the martensitic phase (bcc structure) [45–51] in Fig. 12f, are present in the NiAl intermetallic grains. These have also been found in quenched NiAl thin films [45] and NiAl alloys treated by an air cooling process [49]. The martensitic phase also induced a mismatched crystal plane at the interfaces with the β (B2)-phase, which resulted in partial and complete dislocations, shown in Fig. 12d. These crystallographic irregularities suggest that the nanoscale laminate is rapidly quenched after the reaction. It should be noted that the martensitic transformation in the NiAl intermetallic phase can also be produced by external loading. Park et al. [51] conducted a molecular dynamics calculation which predicted that the fcc (B2) phase in NiAl intermetallic nanowires was transformed into the bcc martensitic phase by tensile strain at a strain rate of 10^9 s^{-1} . However, in this study, due to the longer grain growth time ($\sim 10^{-2}$ s) and fast compression wave propagation time ($\sim 10^{-6}$ s), it is more likely that the martensitic phase was generated by a fast quenching process.

The NiAl₃ phase of the laminates with a 5 μm bilayer thickness shown in Fig. 8c was sectioned and thinned to produce a TEM sample using FIB machining. Figs. 13a and b show atomic scale micrographs from the direct laser shock and the laser-driven, plasma-generated initially shockless compression experiments, respectively. The NiAl₃ phase present in the NiAl microlaminates has

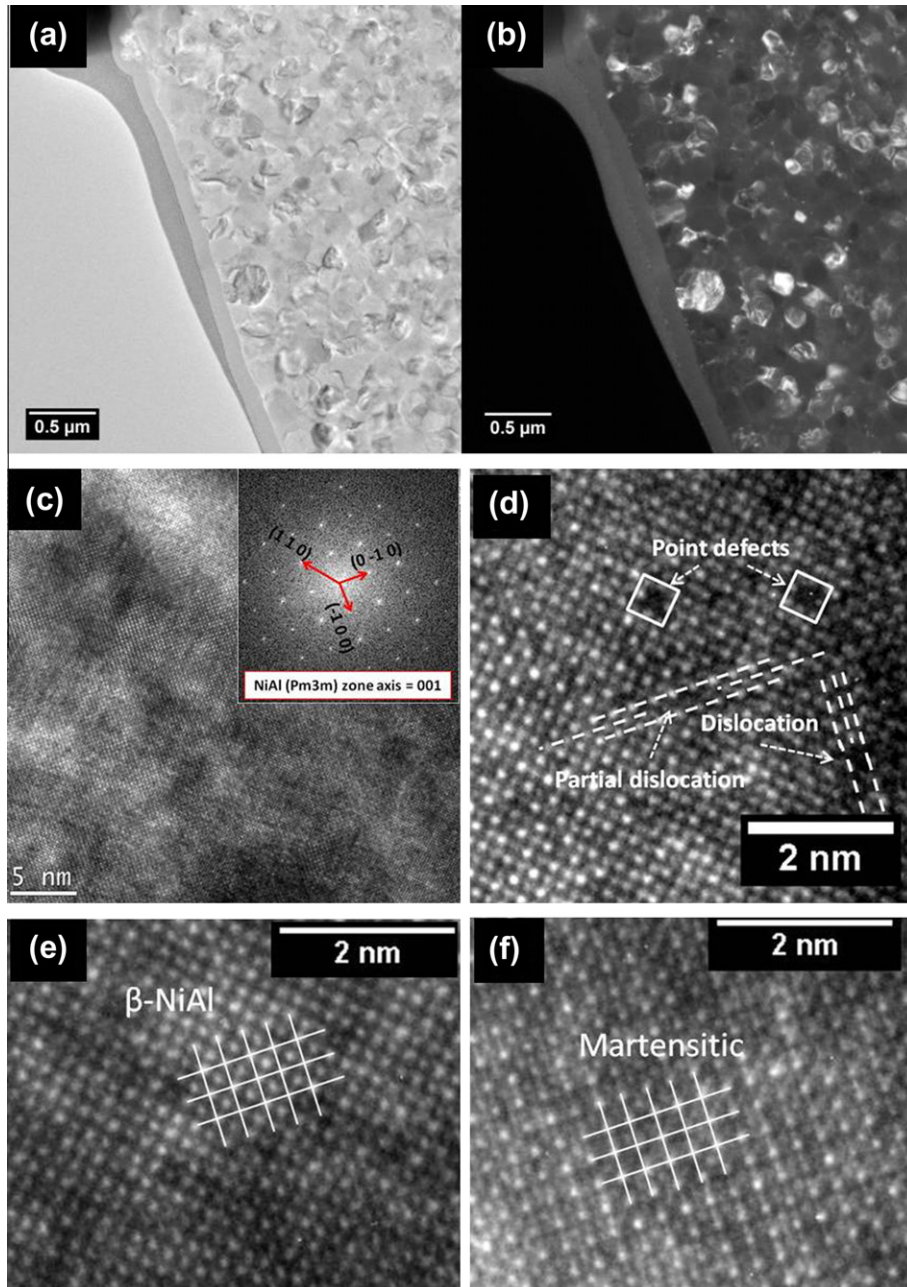


Fig. 12. Atomic resolution TEM structure of reacted Ni/Al nano-laminates: (a, b) bright and dark field images showing NiAl nanoscale grains; (c) atomic image of a single grain with FFT diffraction pattern insert; (d) atomic-micrograph showing lattice defects: vacancy, partial and perfect dislocations in NiAl intermetallic grain; (e) atomic-micrograph of the β phase (fcc) NiAl intermetallic; (f) atomic-micrograph of the NiAl martensitic phase (bcc).

a grain size above $0.5 \mu\text{m}$, the same as in the direct laser shock experiments [13]. However, inside the NiAl_3 grains the structure is quite different from the grains of NiAl intermetallic shown in Fig. 12. Fig. 13a shows an atomic resolution micrograph of the NiAl_3 intermetallic induced by direct laser shock [13]. The size of the mono-crystalline domains is $\sim 7 \text{ nm}$ and the multiple sub-grains produce a FFT pattern with rings of bright dots corresponding to a perfect NiAl_3 crystallographic orientation such as $\{270\}$, the $\{171\}$ surface group and other diffraction spots. There is a large variation in the sub-grain sizes of the

NiAl_3 produced by the laser-driven and initially shockless compression shown in Fig. 13b. The FFT in Fig. 13b shows a few bright spots, such as the $\{123\}$ phase group, and diffuse rings, suggesting that there is only a very small number of areas with a long-range-periodic structure, and a large quantity of amorphous phase. These TEM observations prove that laser-driven initially shockless compression generates a faster quenching rate due to the short laser pulse duration [17,18]. Hence, the formation of long-range periodic atomic structure is difficult in the NiAl_3 phase.

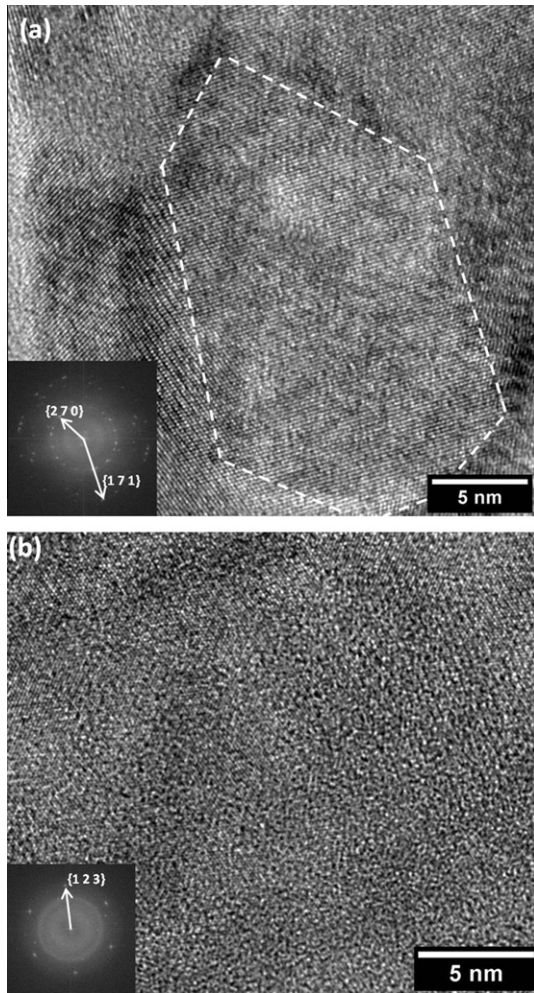


Fig. 13. NiAl₃ intermetallic dendrites in the micro-laminates: (a) direct laser irradiated micro-laminate; (b) laser-driven initially shock-less compression experiment.

4. Conclusions

The use of an innovative laser-driven, shockless compression technique with laser energies of 650, 875 and 1305 J effectively prevented extensive heat damage on the front surface of Ni/Al laminates caused by direct laser irradiation. It also provided a relatively steady shock compression propagating through the entire laminate. The strain rate varied from 10^6 to 10^8 s⁻¹ and peak pressures ranged from 30 to 118 GPa. The strain rate increased as the initially steady loading front gave way to the shock front. The sandwich configuration used provided three regimes:

- microlaminate (~ 5 μ m bilayer thickness) subjected to high amplitude shockless loading on the front face;
- nanolaminate (bilayer thickness ~ 50 nm) subjected to shock compression;
- microlaminate (~ 5 μ m bilayer thickness) subjected to low amplitude shock compression and release, with associated spalling and fragmentation.

In the front face a Ni/Al exothermic reaction with the formation of intermetallic products was initiated by this laser shock technique. However this high temperature reaction was not self-sustaining. The initiation mechanism of the Ni/Al intermetallic reaction is shear deformation between the Ni and Al layers due to the differences in flow stress and bulk compression moduli of Ni and Al. The self-sustaining, high temperature reaction was restrained by the large bilayer thickness and the ambient temperature. This corroborates earlier results for direct laser energy deposition [13].

In the middle layer the nanolaminate fully reacted, producing a fine grain size (~ 500 nm) of NiAl intermetallic. The B2 fcc and martensitic phases of NiAl were observed by atomic resolution electron microscopy. However, the heat generated was insufficient to transmit the reaction to the microlaminates, either in front or back.

The final intermetallic phases have different components, atomic structures and phase distributions that depend on the different laser conditions and quenching processes. The observed martensitic bcc phase is the result of rapid cooling of the fcc (β) NiAl intermetallic.

Acknowledgements

The authors wish to acknowledge the financial support of ONR MURI N00014-07-1-0740. They also thank the Calit2 Nano3 Lab and Scripps Institute of Oceanography for access to carry out the SEM observations. The help with transmission electron microscopy provided by Chia-Hui Lu was extremely valuable. Rain Luo at General Atomics played a key role in the preparation of the assemblies for laser compression. The laser experiments were conducted at the Omega Facility of the Laboratory for Laser Energetics, University of Rochester, through grant DOE NLUF DE-F652-09NA29043. The assistance provided by Dr. B.R. Maddox is gratefully acknowledged. The help by Yung-Chen Lin, Matthew Mechlenburg, and Noah Bodzin at UCLA is also gratefully appreciated.

References

- [1] Wang J, Besnoin E, Knio OM, Weihs TP. Acta Mater 2004;52:5265–74.
- [2] Wang J, Besnoin E, Duckham A, Spey SJ, Reiss ME, Knio OM, et al. Appl Phys Lett 2003;83:3987–9.
- [3] Wang J, Besnoin E, Knio OM, Weihs TP. J Appl Phys 2005;97:114307.
- [4] Miracle DB. Acta Metall Mater 1993;41:649.
- [5] Morsi K. Mater Sci Eng A 2001;299:1–15.
- [6] Kim JS, LaGrange T, Reed BW, Taheri ML, Armstrong MR, King WE, et al. Science 2008;321:1472–5.
- [7] Ma E, Thompson CV, Clevenger LA, Tu KN. Appl Phys Lett 1990;57:1262.
- [8] Blobaum KJ, Van Heerden D, Gavens AJ, Weihs TP. Acta Mater 2003;51:3871–84.
- [9] Gavens AJ, Van Heerden D, Mann AB, Reiss ME, Weihs TP. J Appl Phys 2000;87:1255–63.
- [10] Thadhani NN. Prog Mater Sci 1993;37:117–226.

- [11] Meyers MA, Yu L-H, Vecchio KS. *Acta Metall Mater* 1994;42:715.
- [12] Vecchio KS, Yu L-H, Meyers MA. *Acta Metall Mater* 1994;42:701.
- [13] Wei CT, Maddox BR, Stover AK, Weihs TP, Nesterenko VF, Meyers MA. *Acta Mater* 2011;59:5276–87.
- [14] Van Kessel CGM, Sigel R. *Phys Rev Lett* 1974;33:1020–3.
- [15] Berthe L, Fabbro R, Peyre P, TOLLIER L, Bartnicki E. *J Appl Phys* 1997;82:2826–32.
- [16] Von Allmen M. *Laser-beam interaction with materials*. Berlin: Springer-Verlag; 1987.
- [17] Edwards J, Lorenz KT, Remington BA, Pollaine S, Colvin J, Braun D, et al. *Phys Rev Lett* 2004;92:075002.
- [18] Lorenz KT, Edwards MJ, Jankowski AF, Pollaine SM, Smith RF, Remington BA. *High Energy Density Phys* 2006;2:113–25.
- [19] Schneider MS, Kad BK, Gregori F, Kalantar D, Remington BR, Meyers MA. *Metall Mater Trans A* 2004;35:2633–46.
- [20] Peralta P, DiGiacomo S, Hashemian S, Luo SN, Paisley D, Dickerson R, et al. *Int J Damage Mech* 2009;18:393–413.
- [21] Lu C-H, Remington BA, Maddox BR, Kad B, Park HS, Prisbrey ST, et al. *AIP Conf Proc* 2012;1426:1391–4.
- [22] Lu C-H, Maddox BR, Remington BA, Bringa EM, Kawasaki M, Langdon TG, et al. *AIP Conf Proc* 2012;1426:1387–90.
- [23] Jarmakani H, Maddox BR, Wei CT, Kalantar D, Koniges A, Eder D, et al. *Acta Mater* 2010;58:4604–28.
- [24] Park HS, Lorenz KT, Cavallo RM, Pollaine SM, Prisbrey ST, Rudd RE, et al. *Phys Rev Lett* 2010;104:135504.
- [25] Tierney TE, Swift DC, Luo SN, Niemczura J, Gammei JT, Peralta P. *AIP Conf Proc* 2006;845:1425–8.
- [26] Kalantar DH, Collins GW, Colvin JD, Eggert JH, Hawreliak J, Lorenzana HE, et al. *Int J Impact Eng* 2006;33:343–52.
- [27] Jarmakani HN, Bringa EM, Earhart P, Remington BA, Nhon V, Meyers MA. *Acta Mater* 2008;56:5584–604.
- [28] Loomis E, Peralta P, Swift J, Lim CH, Dickerson R, Dickerson P. *Mater Sci Eng A* 2006;437:212–21.
- [29] Loomis E, Swift D, McNaney J, Lorenzana H, Peralta P. *Acta Mater* 2008;56:3647–62.
- [30] Asay JR. *Int J Impact Eng* 1997;20:27–61.
- [31] Amendt P, Turner RE, Landen OL. *Phys Rev Lett* 2002;89:165001.
- [32] Weihs TP, Reiss M. Method of making reactive multilayer foil and resulting product, US patent no. 6 534 194 (2003).
- [33] Sieber H, Park JS, Weissmuller J, Perepezko JH. *Acta Mater* 2001;49:1139–51.
- [34] Remington BA, Bazan G, Belak J, Bringa E, Caturla M, Colvin JD, et al. *Metall Mater Trans A* 2004;35A:2587–607.
- [35] Remington BA, Allen P, Bringa EM, Hawreliak J, Ho D, Lorenz KT, et al. *Mater Sci Technol* 2006;22:474–88.
- [36] Steinberg DJ, Cochran Marc Meyers SG, Guinan MW. *J Appl Phys* 1980;51:1498–504.
- [37] Sano T, Kato K, Takeishi H. *J Mater Process Technol* 1995;48:391–7.
- [38] Vitali E, Wei CT, Benson DJ, Meyers MA. *Acta Mater* 2011;59:5869–80.
- [39] Okamoto H. *J Phase Equilib Diffus* 2004;25:394.
- [40] Qiu X, Graeter J, Kecskes L, Wang J. *J Mater Res* 2008;23:367–75.
- [41] Gunduz IE, Fadenberger K, Kokonou M, Rebholz C, Doumanidis CC. *Appl Phys Lett* 2008;93:134101.
- [42] Knacke O, Kubaschewski O, Hesselmann K, editors. *Thermochemical properties of inorganic substances*. Berlin: Springer; 1991.
- [43] Nakamura R, Takasawa K, Yamazaki Y, Iijima Y. *Intermetallics* 2002;10:195–204.
- [44] Eyre BL. *J Phys F Metal Phys* 1973;3:422–70.
- [45] Zhang Y, Haynes JA, Pint BA, Wright IG, Lee WY. *Surf Coat Technol* 2003;163–164:19–24.
- [46] Farkas D, Mutasa B, Vailhe C, Ternes K. *Model Simul Mater Sci Eng* 1995;3:201–14.
- [47] Khachatryan AG, Shapiro SM, Semenovskaya S. *Phys Rev B* 1991;43:10832.
- [48] Murthy AS, Goo E. *Acta Metall Mater* 1993;41:2135–42.
- [49] Thompson RJ, Zhao J-C, Hemker KJ. *Intermetallics* 2010;18:796–802.
- [50] Masherghi A, Moshksar MM. *J Alloys Compd* 2009;482:196–8.
- [51] Park HS. *Nano Lett* 2006;6:958–62.